APL Photonics

RESEARCH ARTICLE | OCTOBER 27 2025

Efficient misalignment correction method for dark-field aperture in reflective Fourier ptychographic microscopy

Rui Gao ; Jiasong Sun ; Yao Fan ; Yefeng Shu ; Maciej Trusiak ; Qian Chen ; Chao Zuo

APL Photonics 10, 106124 (2025)
https://doi.org/10.1063/5.0297832

Efficient misalignment correction method for dark-field aperture in reflective Fourier ptychographic microscopy

Cite as: APL Photon. 10, 106124 (2025); doi: 10.1063/5.0297832
Submitted: 21 August 2025 • Accepted: 10 October 2025 •
Published Online: 27 October 2025

View Online Export Citation CrossMark

Rui Gao,[1,2,3] Jiasong Sun,[1,2,3,a)] Yao Fan,[1,2,3] Yefeng Shu,[1,2,3] Maciej Trusiak,[4] Qian Chen,[1,2,3,b)] and Chao Zuo[1,2,3,c)]

AFFILIATIONS

[1] Smart Computational Imaging Laboratory (SCILab), School of Electronic and Optical Engineering, Nanjing University of Science and Technology, Nanjing, Jiangsu Province 210094, China
[2] Smart Computational Imaging Research Institute (SCIRI) of Nanjing University of Science and Technology, Nanjing, Jiangsu Province 210019, China
[3] Jiangsu Key Laboratory of Visual Sensing and Intelligent Perception, Nanjing, Jiangsu Province 210094, China
[4] Warsaw University of Technology, Institute of Micromechanics and Photonics, 8 Sw. A. Boboli Street, Warsaw 02-525, Poland

[a)] **Author to whom correspondence should be addressed:** sunjiasong@njust.edu.cn
[b)] **E-mail:** chenqian@njust.edu.cn
[c)] **E-mail:** zuochao@njust.edu.cn

ABSTRACT

Reflective Fourier ptychographic microscopy (FPM) enables high-resolution, wide-field imaging of opaque surfaces, but its calibration remains challenging due to the unique illumination geometry. Unlike transmissive FPM, which typically employs a regular planar LED array, reflective systems use spatially separated bright-field and dark-field illuminations, with dark-field LEDs arranged around the outer periphery of the objective lens. This non-coplanar, discontinuous configuration invalidates conventional LED calibration methods that generally rely on array continuity or bright-field sub-aperture priors. Here, we propose a non-iterative dark-field misalignment correction method tailored for reflective FPM, referred to as dmc-rFPM. This method formulates a residual cost function based on the structural similarity index between the predicted and measured dark-field intensity images. Each dark-field sub-aperture is independently aligned via heuristic search, and global geometric consistency is enforced using a RANSAC-based circular fitting strategy. This approach eliminates the need for object reconstruction or bright-field-based initialization, supports efficient parallel implementation, and significantly reduces correction time. Simulations and experiments on resolution targets and semiconductor chips demonstrate that dmc-rFPM effectively and precisely corrects 72 dark-field images (each with 400 000 pixels) within 0.5 s using GPU acceleration, achieving a lateral resolution of 583 nm with a 4× objective. dmc-rFPM enables diffraction-limited imaging performance and provides a practical solution for high-throughput calibration in reflective FPM systems for industrial inspection and precision metrology applications.

I. INTRODUCTION

Wide field-of-view (FOV) and high resolution represent a critical imaging requirement in key areas such as life science research, clinical pathology, and industrial non-destructive testing, where comprehensive structural and functional information must be captured without compromising fine spatial details. However, traditional optical systems are fundamentally constrained by the Lagrange invariant, making it difficult to expand the space–bandwidth product (SBP), thereby limiting the amount of information. This poses a significant bottleneck to high-throughput screening and precision diagnostics. To overcome this physical limitation, spatial scanning stitching[1–3] and interferometric synthetic aperture[4–6] have been proposed to extend the SBP. Nonetheless, they

typically rely on complex optical configurations and high-precision mechanical control, resulting in increased system complexity and cost—factors that hinder their applicability in practical scenarios demanding both stability and efficiency.

Fourier ptychographic microscopy (FPM), as a groundbreaking advancement in computational optics, provides a solution for achieving high SBP imaging without significantly increasing hardware complexity. By employing angle-varying plane wave illumination, FPM captures sub-aperture information encoded as lateral shifts in the back focal plane of the objective lens. These multiplexed frequency components are synthesized via alternating projections, enabling the reconstruction of high-resolution images that surpass the native numerical aperture (NA) limit of the objective lens. Since it was proposed by Zheng *et al.*,[7] this technique has undergone continuous advancements in systematic error correction,[8–11] resolution enhancement,[12,13] reconstruction efficiency,[14,15] and system robustness.[16,17] Consequently, FPM has been widely applied in critical fields such as biomedical imaging,[18,19] pathological analysis,[20] and industrial non-destructive testing.[21–23]

Depending on sample characteristics and application requirements, FPM systems can be classified into transmissive[24] and reflective[25] modalities. Transmissive FPM is optimized for transparent or weakly absorbing specimens, while reflective FPM extends applicability to opaque or highly reflective materials such as metals, semiconductors, and ceramics, thus offering broader material compatibility. In contrast to transmissive FPM, which typically employs densely packed, regularly arranged LED arrays to facilitate accurate control of illumination angles and positions, reflective FPM relies on two spatially separated light sources to generate bright-field and dark-field illumination, respectively. This sparse configuration lacks both spatial continuity and structural correlation between bright-field and dark-field illumination, posing substantial challenges for precise system correction. Consequently, illumination source misalignments lead to incorrect sampling of spatial frequency components, resulting in information mismatches during frequency-domain stitching. These artifacts significantly degrade image reconstruction quality and are especially detrimental in reflective FPM. It has emerged as a critical bottleneck, limiting its high-resolution imaging performance.

Although methods such as the pcFPM[26] based on global geometric optimization and the efficient self-calibration strategy[27] based on spectrum autocorrelation have demonstrated accurate LED position estimation within the bright-field spectrum for transmissive FPM, these approaches critically rely on the assumption of continuous illumination sources and thus are not readily applicable to reflective imaging dominated by dark-field illumination with discrete lighting configurations. Reported methods for correcting dark-field aperture misalignment in reflective FPM remain relatively limited.[10,11] Although these approaches take into account the discontinuous arrangement of bright-field and dark-field illuminations in reflective FPM systems, the correction strategies employed are largely derived from methods originally designed for transmissive FPM. Therefore, these techniques still require iterative reconstruction of the full object information. The aperture position corresponds to the LED illumination angle, which is relatively stable and less susceptible to the environment. Thus, treating its correction as an independent preprocessing step can reduce the algorithm's complexity. In particular, reflective FPM faces four fundamental challenges in dark-field imaging. First, the spatial positions of dark-field LEDs are largely uncorrelated with those of bright-field sources, resulting in a significantly higher degree of freedom for calibration. In addition, the sparse and discrete arrangement of LEDs prevents the application of continuity-based constraints commonly used in transmissive systems. Moreover, the dark-field spectral boundaries in reflective FPM tend to be blurred, which necessitates computationally intensive iterative reconstruction of complex amplitudes in traditional calibration approaches. Compounding these difficulties, the inherently low signal-to-noise ratio of reflective imaging further amplifies the sensitivity to sub-aperture misalignments in the frequency domain, thereby severely compromising reconstruction accuracy. Therefore, developing an efficient LED position correction method that does not require dark-field iterative reconstruction and is suitable for discrete source structures is of great significance for improving the imaging performance and practicality of reflective FPM.

To address the aforementioned challenges, this paper proposes a structural similarity (SSIM)[28]-based fast dark-field aperture misalignment correction method—dark-field misalignment correction for reflective FPM (dmc-rFPM). By constructing a dark-field intensity estimation model that incorporates the effects of aberrations, noise, and positioning errors and by introducing the aberration compensation strategy for annular illumination in transmissive FPM into reflective imaging tasks for the first time, the intensity distortion caused by aberrations is eliminated. Meanwhile, the wavelet transform is employed to suppress the inherent noise interference in dark-field images, while the structural similarity between the estimated and measured images is evaluated using SSIM. Combined with the random sample consensus[29] (RANSAC) spatial fitting algorithm to robustly position sub-apertures in the Fourier domain, the positioning parameters of each dark-field LED are accurately deduced. This method eliminates the need for iterative reconstruction, significantly improving the positioning efficiency of dark-field sub-apertures while maintaining high precision. Simulations and experiments demonstrate that the dmc-rFPM enables stable and efficient correction of dark-field sub-aperture positions in the Fourier domain. Compared to existing strategies, the overall processing speed is increased by approximately fivefold, with a minimum requirement of only four sub-apertures, and achieves correction times at the 0.5-s level under Graphics Processing Unit (GPU) parallel acceleration. This method provides critical support for the rapid deployment and robust operation of reflective FPM, extending its application boundaries in complex material imaging and real-time inspection.

II. SYSTEMS AND METHODS

A. Reflective FPM system

The experimental system in this study was modified based on an existing NEXCOPE NE950 microscope. The modification involved only two LED modules and mounting brackets, transforming the original fluorescence illumination path into a customized metallographic bright-field illumination light path. As shown in Fig. 1(a), the ring-shaped LED array is positioned at the aperture plane and precisely aligned to achieve multi-angle oblique illumination via discrete quasi-plane waves. The maximum illumination angle provided matches the NA angle of the objective lens

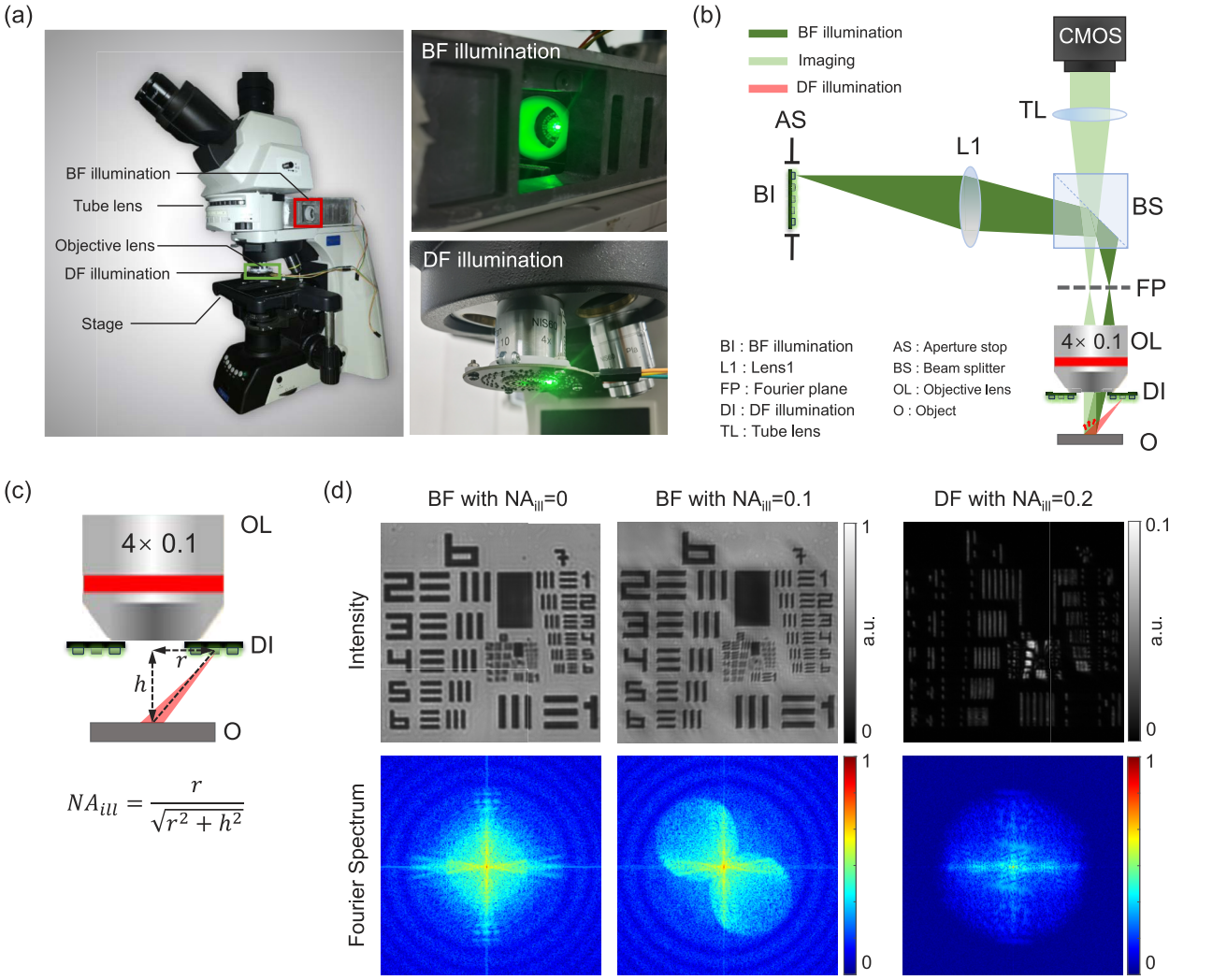

FIG. 1. Experimental setup and image acquired. (a1) Experimental setup with bright-field/dark-field illumination. (b) Optical path diagram. (c) Calculation method for dark-field illumination NA. (d) Acquired intensity images for bright-field vertical illumination (NA_{ill} = 0), oblique illumination (NA_{ill} = 0.1), and dark-field illumination (NA_{ill} = 0.2), with the corresponding spectrum.

(NIS60, 4×, NA = 0.1), enabling bright-field spectrum reconstruction with a cutoff frequency of $2NA_{obj}/\lambda$ using only a few captured bright-field images.[30] The ring-shaped illumination configuration effectively ensures high SNR acquisition of low-frequency information while maintaining broad frequency coverage (up to 2NA). The dark-field illumination module consists of 72 discrete LEDs mounted on the outer cylindrical surface of the objective, providing dark-field illumination with a NA of 0.36. Specific illumination parameters are provided in Table I. Thus, the system achieves a synthetic NA of 0.46 by acquiring 80 images. This configuration satisfies the minimum 40% spectrum overlap requirement, ensuring sufficient overlap between dark-field and bright-field spectra to guarantee both the convergence of iterative algorithms and the accuracy of the reconstructed results.

Figure 1(b) illustrates the optical path of the system. Light emitted from the bright-field LED (central wavelength: 522 nm, spectral bandwidth: 30 nm) is focused by relay lenses onto the back focal plane of the objective, forming collimated illumination on the sample. The reflected light is then converged through the objective and tube lens onto the detector (a monochrome CMOS, The Imaging Source DMK 24UJ003, with 1.67 μm pixel size) to form

TABLE I. Illumination parameters.

Ring No.	Radius (mm)	Illumination (NA)	Number of LEDs
Bright-field	5.5	0.10	8
Dark-field I	5.7	0.20	16
Dark-field II	8.7	0.30	24
Dark-field III	10.7	0.36	32

bright-field images. Meanwhile, the dark-field LEDs illuminate the sample directly, with scattered light being collected by the objective and tube lens to form dark-field images. Figure 1(d) demonstrates the intensity and spectrum characteristics of both bright-field and dark-field images under different illumination NA. The results confirm that bright-field illumination angle matching the objective NA achieves high-fidelity acquisition of low-frequency information, while wide-angle dark-field illumination extends the spectrum coverage range, supporting high-quality reconstruction in reflective FPM.

B. Intensity model and algorithm principle

In FPM, the sample information is modulated by multi-angle illumination and encoded in the acquired intensity images. The system varies the illumination angles to shift the object spectrum $O(\boldsymbol{k})$ in the frequency domain using the illumination wavevector as the displacement factor. The pupil function $P(\boldsymbol{k})$ serves as a frequency-domain probe, enabling the acquisition of multiple low-resolution spectra that collectively cover the entire spectrum range. Here, m, n represent the spatial index coordinates of the 2D LED array. The captured spectrum undergoes an inverse Fourier transform $\mathscr{F}^{-1}$, and its modulus squared yields the corresponding low-resolution intensity image, which is then matched with the acquired image.

Ideally, the acquisition intensity constraint should be accurately applied to the sub-aperture spectrum corresponding to the illumination angle. However, LED illumination angle positioning errors can cause misalignment between the estimated sub-aperture and the actual imaging sub-aperture, thereby introducing significant reconstruction errors. Meanwhile, factors such as system aberrations and detection noise can further exacerbate the inconsistency between the estimated and acquired intensity images. To accurately model the intensity image formation process in practical systems, a comprehensive intensity model is introduced that accounts for sub-aperture misalignment, system aberrations, and noise in an intensity generation framework, expressed as follows:

$$I(\boldsymbol{r}) = \left|\mathscr{F}^{-1}\left[P(\boldsymbol{k})e^{i\phi(\boldsymbol{k})}O(\boldsymbol{k}-\boldsymbol{k}_{m,n})\right]\right|^2 + I_{\text{noise}}, \tag{1}$$

where $\boldsymbol{r}$ denotes the spatial coordinate vector and $\phi(\boldsymbol{k})$ represents the system aberration term, expressed as a linear combination of Zernike polynomials $z_0^0 + z_1^{\pm1} + z_2^0 + z_2^{\pm2} + \cdots + z_n^m$, which characterizes the wavefront distortion in the actual pupil function. $k_{m,n}$ denotes the illumination wavevector corresponding to the (m, n)-th LED, and I_{noise} represents the noise term.

To isolate the dominant effect of LED position errors in intensity discrepancies, we first apply a sub-aperture registration algorithm and the bright-field aberration correction method[27,31] to eliminate fitting errors caused by system aberrations. Prior studies have demonstrated that employing annular illumination matching the objective's NA in transmissive FPM provides sufficient information for simultaneous object information reconstruction and adaptive aberration estimation.[31] Building on this strategy, we introduce NA-matched illumination to reflective FPM, enabling efficient system aberration recovery and correction in the reflection pathway. By incorporating the reconstructed system aberrations into the dark-field intensity estimation model, we significantly enhance model fitting accuracy while effectively suppressing aberration-induced intensity discrepancies. Furthermore, to address the noise sensitivity of dark-field images, we introduce a wavelet-domain based denoising and background suppression algorithm,[32] which effectively eliminates errors from dark current and environmental interference. The synergistic implementation of these strategies significantly enhances the reliability of the intensity model, ensuring that cost function residuals primarily reflect sub-aperture displacement errors, thereby establishing a robust foundation for accurate LED position error estimation.

To achieve precise aperture positioning, we introduce SSIM as the optimization criterion for image error evaluation. SSIM comprehensively evaluates image similarity through analysis in three dimensions of luminance, contrast, and structural features, with a particular emphasis on local structure preservation capability. However, since dark-field images contain a large number of pixels with values close to zero, invalid data may be generated. To mitigate this effect, this paper optimizes the SSIM algorithm by excluding pixels with near-zero values in both dark-field images from the calculation, thereby expanding the dynamic range of SSIM values,

$$SSIM(x,y) = H\left(\tau - \frac{1}{N}\sum_{k=1}^{N}\mathbb{I}(x_k = 0 \vee y_k = 0)\right) \times \frac{(2\mu_x\mu_y + C_1)(2\delta_{xy} + C_2)}{(\mu_x^2 + \mu_y^2 + C_1)(\sigma_x^2 + \sigma_y^2 + C_2)}. \tag{2}$$

$H(\cdot)$ is the Heaviside-step function ($H(a) = 1$ when $a > 0$, otherwise $H(a) = 0$); τ is used as a threshold to exclude subsets with an excessive number of near-zero pixels, thereby enhancing the dynamic range of the global SSIM value. The specific value of τ is determined based on the statistical distribution of the proportion of near-zero pixels across all subsets during the actual SSIM calculation for the images. N is the total number of pixels; $\mathbb{I}(\cdot)$ is the indicator function (equal to 1 if the condition is satisfied, otherwise 0); and x_k and y_k are the pixel values of the two images. When the proportion of zero-valued pixels exceeds τ, the corresponding SSIM value is discarded. Then, x, y denote two registered images; μ_x, μ_y denote the mean of the image vector; σ_x, σ_y denote the standard deviation of the image vector; and δ_{xy} denotes the covariance of the image vector. To prevent division by zero, constants C_1 and C_2 are introduced.

Dark-field images typically exhibit high contrast, low SNR, and prominent structural details, making their matching process rely more on local structural features rather than absolute intensity values. Therefore, SSIM demonstrates higher robustness and sensitivity in characterizing structural differences between dark-field images, making it particularly suitable for the precise estimation of the frequency-domain aperture position.[33] Consequently, the optimal solution for dark-field aperture positioning should satisfy

$$\min_{\Delta k}\mathscr{L}_{\text{SSIM}} = \min_{\Delta k}\left(1 - \text{SSIM}(I, \gamma \cdot I(r; \Delta k))\right). \tag{3}$$

Δk represents the spatial frequency position in the search. This strategy achieves a high-precision inversion of the actual position of the dark-field illumination aperture by maximizing the structural similarity between the estimated image $I(r;\ \Delta k)$ and the measured image I, providing critical support for subsequent spectrum stitching and high-resolution reconstruction. It should be noted that estimating the dark-field image using bright-field reconstruction will suffer from missing frequency spectrum information, typically resulting in an overall brightness lower than that of the measured

image. To mitigate the influence of the luminance component on SSIM evaluation, an intensity correction factor γ is introduced, calculated as the ratio of average intensities between the captured and estimated images. In Figs. 4(b1)–4(b3), the distribution of SSIM values under different levels of Gaussian noise with and without intensity correction is simulated. This processing ensures that the image structure becomes the dominant factor in the comparison, leading to a more stable correction procedure.

C. dmc-rFPM method

By utilizing SSIM as an evaluation metric, dmc-rFPM can accurately position the dark-field aperture without reconstructing the dark-field spectrum of the object, eliminating iterative reconstruction during the correction process. Figure 2 illustrates the entire correction procedure, using the annular LED board as a demonstration.

Prior to formally initiating the method, acquiring the accurate bright-field spectrum is essential. Initially, sequentially activate the eight LEDs located at the edge of the bright-field LED illumination ring to acquire eight bright-field images. Subsequently, we use edge detection[27] to identify the location of the bright-field sub-aperture in the frequency domain. Then, we perform bright-field information reconstruction and aberration correction.[31] The system's pupil function constitutes a bandpass function with a radius of NA/λ. We compute the initial estimation of the dark-field sub-aperture's center based on the LED ring's physical dimensions and the objective working distance. At this stage, the initialization process is complete; we now shift to the positioning procedure. First, the initial estimation is used as the center, and the aperture is simultaneously translated in four directions (up, down, left, and right) by a predetermined step size, as shown in Fig. 1 "aperture shift." According to the dark-field intensity estimation model in Eq. (1), five estimated intensity images $I_n(r;\ \Delta k)\ (n = 1, 2, \ldots, 5)$ containing initial positions can be obtained. After intensity correction of the estimated intensity images, the true dark-field sub-aperture position corresponds to the frequency-domain shift Δk that maximizes the SSIM value between the estimated intensity $I_n(r;\ \Delta k)$ and the detector-captured intensity I, using Eq. (3) as the cost function. Since the correction of each sub-aperture is independent, all dark-field sub-apertures on a

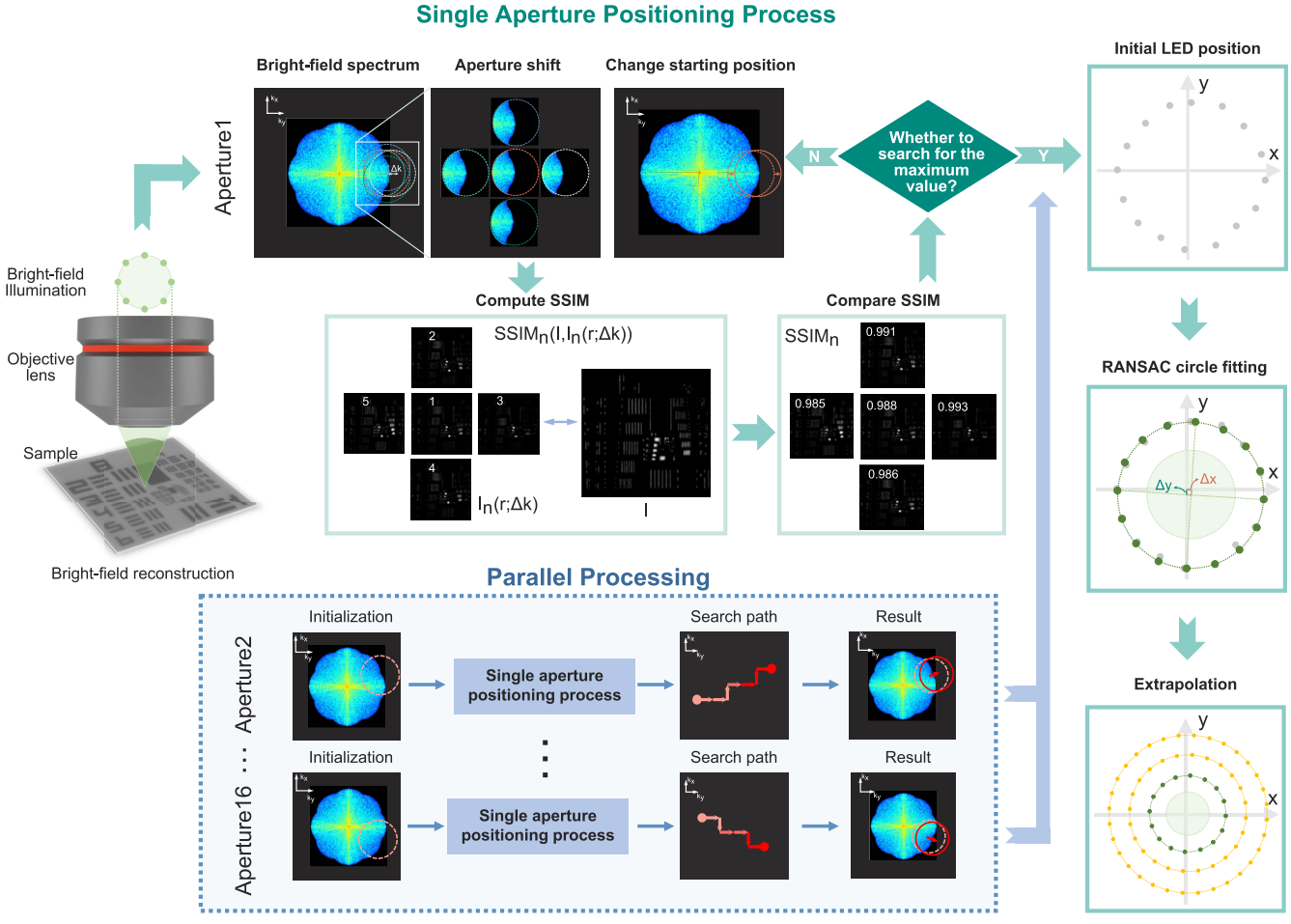

FIG. 2. Flow chart of dmc-rFPM.

single ring can be corrected simultaneously. However, variations in the quality of the acquired dark-field images may introduce outliers in the results. To eliminate these outliers, the overall LED annular light band can serve as a constraint. The RANSAC algorithm is then employed to fit the centers of the dark-field apertures to a circle, determining the radius and center of the circle where the first circle of dark-field aperture centers is located. The rotation angle of the LED board is determined by tracking a fixed dark-field sub-aperture center point throughout the circle fitting procedure. Calculate the slope k_1 of the line connecting this point to the center of the fitted circle. Simultaneously, determine the slope k_2 of the line extending from this point to the theoretical (without positional errors) circle's center. The LED board's actual rotation angle θ then derives from

$$\theta = \arctan \frac{|k_2 - k_1|}{|1 + k_1 k_2|}. \tag{4}$$

Finally, following the LED arrangement rule, the central positions of the remaining dark-field sub-apertures are determined by extrapolating those of the first circle of dark-field sub-apertures, thus completing all correction steps. The component placement accuracy error in modern Surface Mounted Technology (SMT) typically ranges from ±50 to ±100 μm. With consistent system parameters, this error, on a 600 × 600 pixel^2 image, results in an offset of ~0.7 to 1.4 pixels in spectrum, exerting negligible influence on the final correction outcome. However, outlier errors can induce frequency spectral offsets far exceeding 1 pixel. Consequently, the sub-aperture center corresponding to the LED trajectory in the frequency domain can be treated as an ideal circle for fitting purposes in an ideal imaging system, disregarding Printed Circuit Board (PCB) processing errors.

III. SIMULATIONS

A. Method effectiveness

The validity of dmc-rFPM must be assessed before its application to actual experimental data. This section aims to evaluate the characteristics of the residual distribution of the cost function through simulation. The simulated system data are the same as the experimental system data presented in Sec. II A. The simulated amplitude and phase correspond to "cameraman" and "westconcordaerial." The simulated image dimensions are 631 × 631 pixel^2. The radius of the first circle of dark-field LEDs is 5.7 mm,

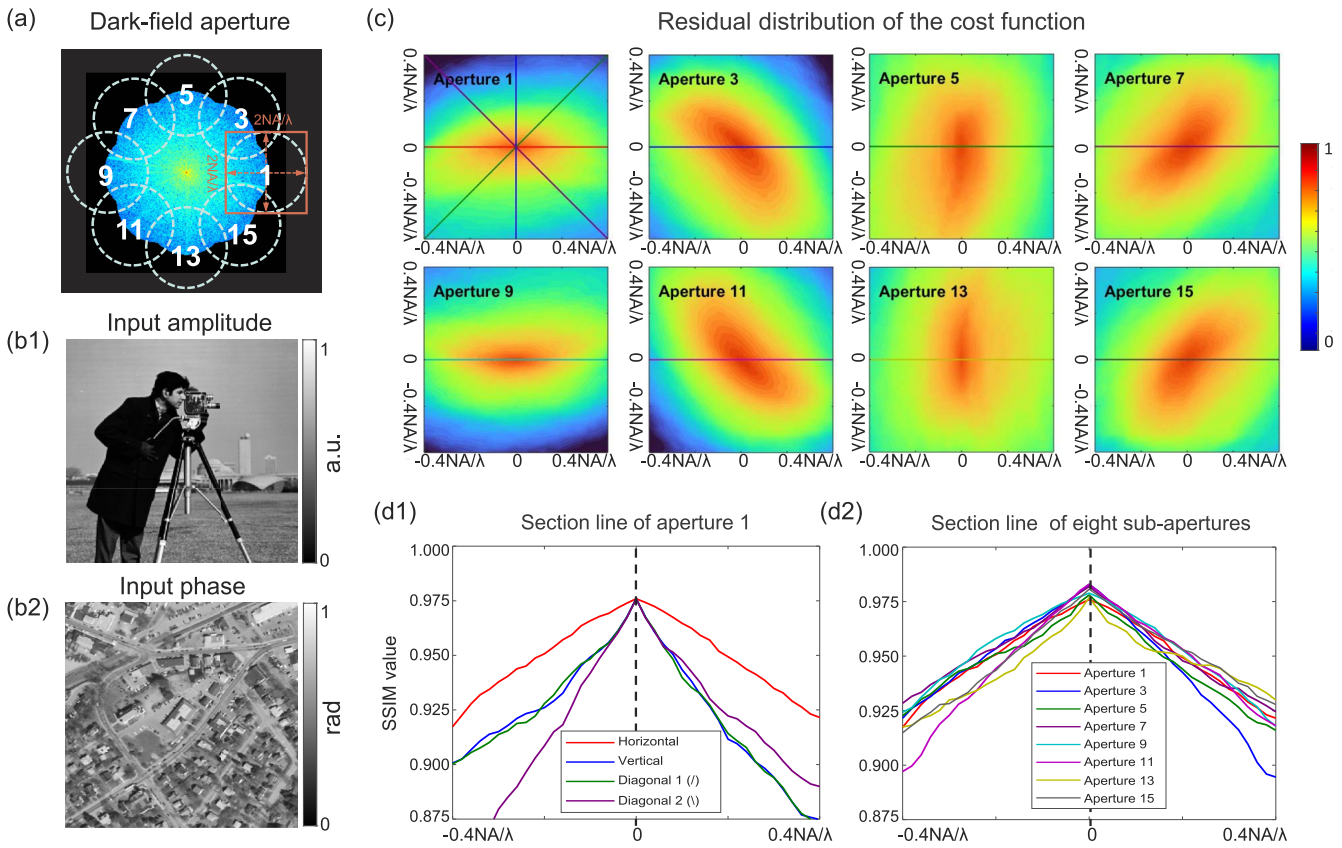

FIG. 3. Residual distribution characteristics of the dmc-rFPM cost function. (a) Dark-field aperture in the first circle. (b1) and (b2) Simulated amplitude and phase, respectively. (c) Residual distribution of the cost function for eight sub-apertures in the integer pixel direction. (d1) Section lines of the cost function for aperture 1 in four orthogonal directions. (d2) Section lines of the cost function for eight sub-apertures in (a).

with a corresponding illumination NA of 0.2. The dark-field light source is segmented into 16 equal parts along the circle to offer adjustable illumination angles. Three errors can occur in the dark-field LED board within a real system: (1) the height Δh of the light source from the object; (2) the lateral translations Δx and Δy of the LED board; and (3) the rotation angle θ of the LED board. These errors manifest as lateral translations of the sub-aperture center in the frequency domain. Assuming that the 16 dark sub-apertures with an illumination NA of 0.2 are actual sub-apertures, and the aperture center is positioned at (0, 0) point, calculating SSIM values between the estimated intensity images and the simulated real intensity images at various positions ($\pm 0.4NA_{obj}/\lambda$ range in x and y) consequently determines the residual distribution of the cost function for a single sub-aperture. Eight representative sub-apertures positioned at 45° intervals were chosen for analysis based on the frequency spectral distribution characteristics, as depicted in Fig. 3(c). The pseudo-color diagram in Fig. 3(c) illustrates a gradual decrease in residual error of the cost function from the central highest point toward the periphery. Each individual sub-aperture exhibits a unique global maximum value in the residual error distribution of the dmc-rFPM cost function, with this maximum value corresponding to the true center position of the sub-aperture. This distribution pattern ensures the precision of the dmc-rFPM correction. The dmc-rFPM provides a unique global solution, achievable by using a straightforward search strategy for convergence. Figures 3(d1) and 3(d2) show that the section lines of aperture 1 in four orthogonal directions each exhibit a unique global maximum, with all maxima precisely coalescing at x = 0. Although the section lines of the eight sub-apertures exhibit amplitude variations, their peak positions remain consistently fixed at x = 0.

B. Noise effects

The absence of the zero-frequency diffraction signal renders dark-field intensity images vulnerable to noise interference, thereby undermining the precision of algorithmic corrections. To enhance the signal-to-noise ratio during the acquisition of dark-field micrographs, it is frequently imperative to shield from external light sources by a light barrier, establishing a darkroom environment. Specifically for metallographic samples, noise interference becomes more obvious due to the varying reflectivity across the sample surface. A simulation was conducted to assess the impact of noise on the correction capability of dmc-rFPM. Aperture 1 in Fig. 3(a) was selected as an example for this analysis. The simulation maintained complete consistency in system parameters, object information, and the coordinates of residual distribution within the cost function. Figure 4(a) illustrates a comparison of dark-field intensity images when introducing Gaussian noise of varying intensities and threshold denoising,[32] without any shift in the sub-aperture centers. Increasing noise intensity can result in the threshold denoising filtering out effective information in the image, as indicated by the red arrow in Fig. 4(a), leading to inaccurate SSIM assessment outcomes. The residual distributions of the cost function are compared in three different noise levels to provide a more comprehensive illustration of the impact of noise and intensity correction on the correction results: (1) without intensity correction and threshold denoising, as shown in Fig. 4(b1); (2) with intensity correction but no threshold denoising, as shown in Fig. 4(b2); and (3) with both intensity correction and threshold denoising, as shown in Fig. 4(b3). These representations display the cost function's section lines within the range of $\pm NA_{obj}/\lambda$, centered on the true sub-aperture. Assuming that Gaussian noise is the noise present during the acquisition of the dark-field intensity images, this noise is categorized into ten levels, with the standard deviation σ ranging from 10^{-3} to 10^{-2}. Figure 4(b2) illustrates that when only intensity correction is applied, images with minimal noise exhibit a unique global maximum value in the residual distribution of the cost function, indicating the algorithm's correction capability. Nevertheless, as the noise intensity escalates, the cost function ceases to possess a global

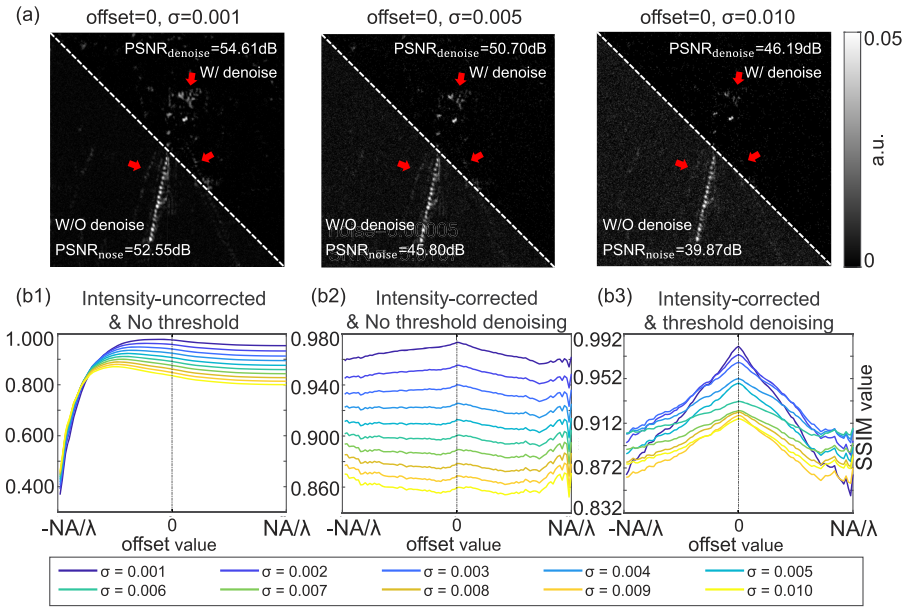

FIG. 4. Effects of dark-field noise and intensity correction on the correction capability of dmc-rFPM. (a) Comparison of dark-field intensity images with varying Gaussian noise levels (σ = 0.001, 0.005, 0.01) when the sub-aperture center is at the edge of the bright-field spectrum (offset = 0), alongside results after threshold denoising. (b) Residual distribution curves of the cost function under different noise intensities and image processing methods: (b1) intensity uncorrected and no threshold denoising, (b2) intensity corrected and no threshold denoising, and (b3) intensity corrected and threshold denoising.

unique maximum value starting at a Gaussian noise standard deviation of σ = 0.004, leading to a loss of correction ability by the algorithm. After threshold denoising and intensity correction of the dark-field intensity image, all cost functions exhibit globally unique maximum values, enabling the algorithm to acquire accurate results, as shown in Fig. (b3). Conversely, as illustrated in Fig. 4(b1), when no processing is applied to the estimated dark-field intensity images, the cost function demonstrates monotonic behavior as the sub-aperture approaches the center of the low-spectrum. However, as the sub-aperture moves away from the center of the low-spectrum, the cost function changes gradually, lacking a globally unique maximum value, thereby impeding the algorithm's correction capability. In addition, excessive noise in the dark-field image in FPM adversely impacts reconstruction quality[25] and compromises the correction accuracy of dmc-rFPM. Therefore, dmc-rFPM requires the same prerequisites as FPM reconstruction, ensuring that the system's robustness remains uncompromised.

C. Method stability and simplification

Due to the periodic arrangement of the LEDs, the position of all dark-field sub-aperture centers can be determined by identifying the circle on which they lie in the frequency domain. Mathematically, defining a circle requires a minimum of three non-collinear points. Previous analysis has shown that dmc-rFPM effectively corrects for eight sub-apertures positioned at 45° intervals (specifically sub-apertures 1, 3, 5, 7, 9, 11, 13, and 15), offering complete directional and maintaining pixel-level accuracy. In addition, the number of sub-apertures can be reduced to four (sub-apertures 1, 5, 9, and 13) to correspond to the cardinal directions, depending on specific needs. Increasing computational data processing throughput positively correlates with the reduction in the number of apertures. Therefore, reducing the number of apertures can conserve computing resources, enhance correction speed, and improve method adaptability across varying computational capacities. The method can be categorized into three versions based on the number of sub-apertures: (1) 16 LEDs at 22.5° intervals, (2) 8 LEDs at 45° intervals, and (3) 4 LEDs at 90° intervals.

To simulate true application conditions, random errors are introduced to the LED pose, and three versions of the correction method are applied to assess the stability and robustness of dmc-rFPM. Using actual system parameters as a benchmark, the rotation angle range $\theta \in [0°, 1°, 3°, 5°]$, height error range $\Delta h \in [-5, 5\ \text{mm}]$, and lateral translation range $\Delta x \in [-1, 1\ \text{mm}]$, $\Delta y \in [-1, 1\ \text{mm}]$ are defined as error parameters. When the LED light source adjustment error surpasses these ranges, the deviation becomes pronounced, necessitating initial visual manual correction. This study utilizes open datasets of metallographic samples[34,35] for simulating real objects to assess correction efficacy. These datasets comprise PCB samples, semiconductor samples, and metal surface defects. We selected 100 sets of random error parameters, which were randomly applied to different samples. Three method versions were executed to correct these samples, evaluating their correction performance and determining their applicable ranges. Calculate the Euclidean distance between the correction results and the ground truths, examining the correction outcomes of the lateral translation error $\sqrt{(\Delta x)^2 + (\Delta y)^2}$, height error Δh, and angle error θ. The data distribution is illustrated through box plots in Figs. 5(a)–5(c). Statistical analysis indicates that fewer LEDs used for correction result in a larger overall rotation angle and diminished error suppression by the method. Despite some deviation, the error distribution remains acceptable. In particular, the deviation in the final correction is maintained within 0.1 and 0.2 mm, rendering its impact on the reconstruction results negligible.

D. Time consumption

For the absence of a universal correction method for dark-field sub-aperture in reflective FPM systems, we compared the

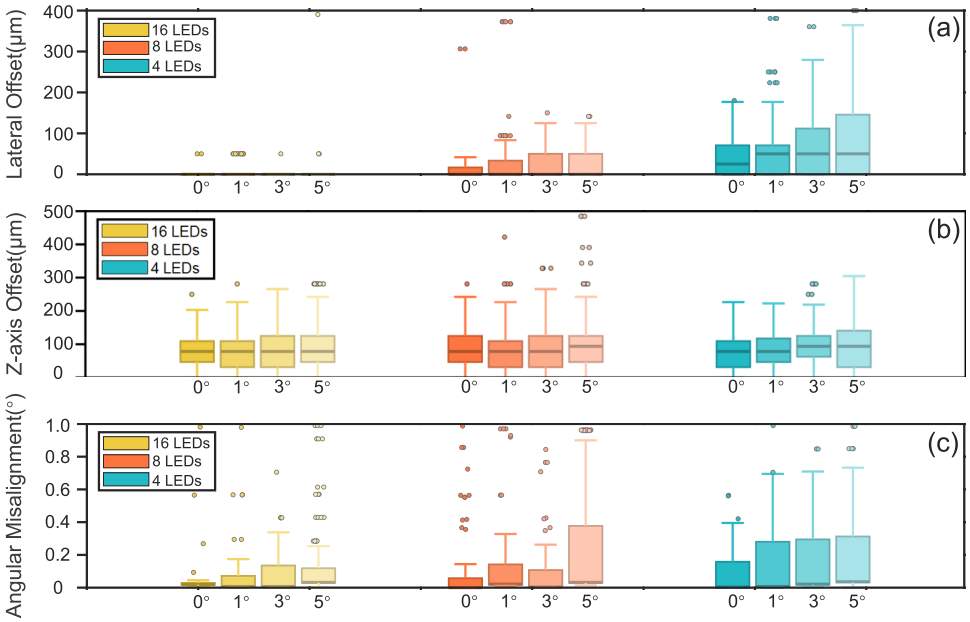

FIG. 5. Correction capability of three dmc-rFPM versions measured by the Euclidean distance between the correction results and ground truths using varying numbers of LEDs: (a) lateral translation error $\sqrt{(\Delta x)^2 + (\Delta y)^2}$, (b) height error Δh, and (c) rotation angle error θ.

TABLE II. Comparison of several correction methods.

Methods	pcFPM	Efficient self-cal	dmc-rFPM I
Time cost (s)	104.2	83.4	22.6
Methods	dmc-rFPM II	dmc-rFPM III	
Time cost (s)	10.2	4.5	

reconstruction times of two classical sub-aperture correction methods originally designed for transmissive FPM, referred to as pcFPM[26] and efficient self-calibration.[27] The correction involves 8 bright-field LEDs and 72 dark-field LEDs, with all other system parameters matching the previously mentioned simulation data. The algorithms dmc-rFPM I, dmc-rFPM II, and dmc-rFPM III in this study utilize correction methods with 16, 8, and 4 LEDs. Simulations were conducted on a platform with an AMD Ryzen 7 6800HS processor (3.2 GHz, integrated Radeon 680M graphics) and 16 GB DDR4 memory, using MATLAB R2023a for implementation. As shown in Table II, dmc-rFPM significantly reduces the processing time compared to conventional methods. Fewer LEDs further reduce the time required, and GPU acceleration allows the correction time to reach as fast as 0.5 s.

IV. EXPERIMENTS

A. Resolution validation using USAF target

Compared to simulations, real system errors are more intricate. Simulations only model the primary anticipated errors. Therefore, it is imperative to validate the stability and robustness of the

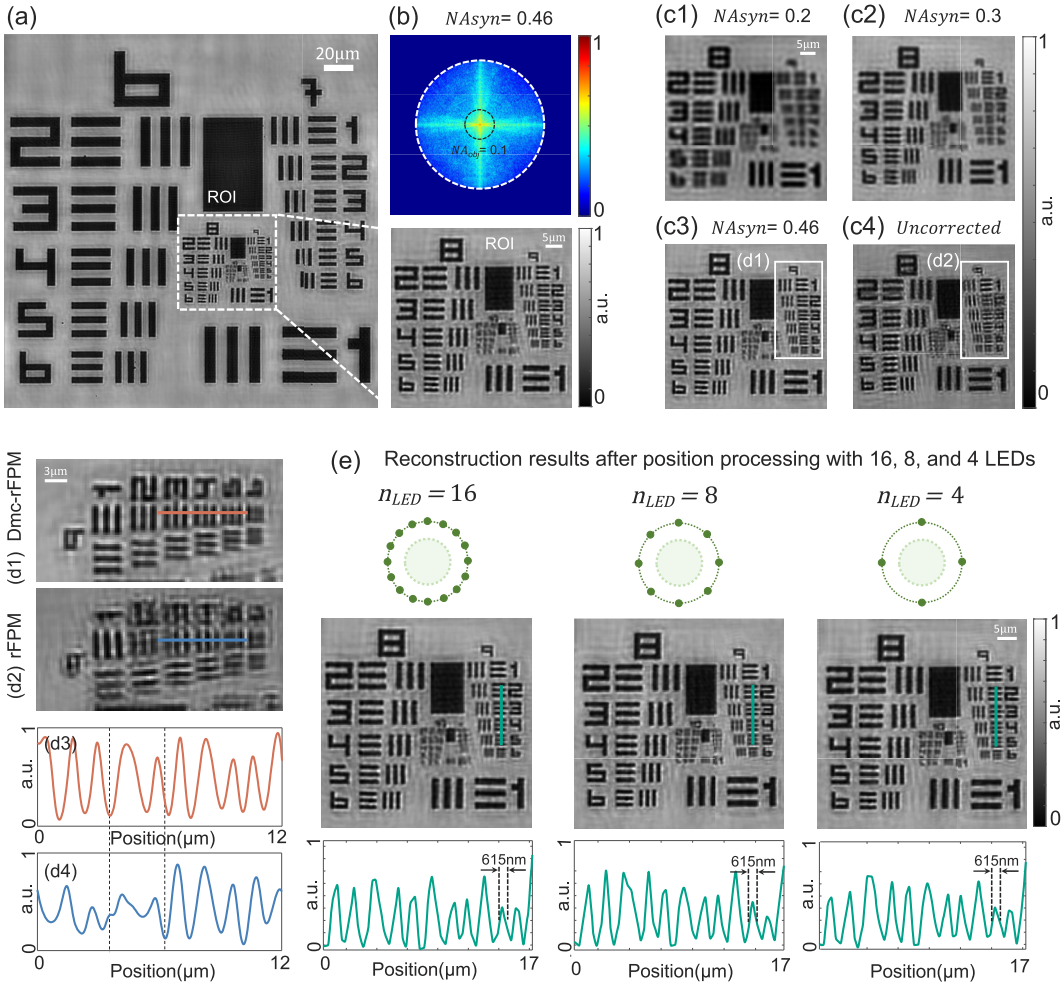

FIG. 6. Tested outcomes of the USAF target. (a) Reconstruction results for the USAF target using the corrected equivalent synthetic aperture NA_{syn} = 0.46. (b) Reconstructed spectrum. (c) Intensity outcomes for the USAF target from group 8 to group 11 under varying conditions: (c1) reconstruction using only bright-field information (NA_{syn} = 0.2), (c2) reconstruction using dark-field information from the first circle (NA_{syn} = 0.3), (c3) reconstruction using all dark-field information (NA_{syn} = 0.46), and (c4) reconstruction result for dark-field sub-aperture without position processing. (d) Enlarged details from the white boxes in (c3) and (c4), and corresponding section lines (element 3–element 5 in group 9). (e) Reconstruction results for groups 8 to 11 after position processing with 16, 8, and 4 LEDs, including section lines of local patterns.

system and method presented in this study through real experiments. The experiment utilized a microscope with bright-field and dark-field illumination, depicted in Fig. 1, with system parameters consistent with those outlined in Sec. II A. To assess the imaging reconstruction efficacy pre- and post-dmc-rFPM correction, FPM reconstruction was conducted with and without dark-field aperture calibration on the 6th to 11th fringe groups of the USAF target during the experiments. The outcomes are illustrated in Figs. 6(c3) and 6(c4), respectively. Notably, Fig. 6(c4) exhibits clear artifacts. Figures 6(d1) and 6(d2) present the magnified views of the pattern in group 9 from Figs. 6(c3) and 6(c4). Figures 6(d3) and 6(d4) present the section lines of transverse patterns from element 2 to element 5 in group 9, respectively. The contrast in the segment associated with the system's limit resolution, indicated by the curve in Fig. 6(d4), diminishes and fails to be fully resolved. Consequently, if the dark-field aperture position in the reconstruction model is incorrect, the quality of FPM reconstruction significantly deteriorates, markedly reducing the system's limit resolution. Then, we analyzed the enhancement of the system's highest resolution through dark-field imaging data. Figures 6(c1)–6(c3) display intensity results for bright-field information reconstruction alone (NA_{syn} = 0.2), incorporation of the first circle of dark-field information (NA_{syn} = 0.3), and full dark-field information reconstruction (NA_{syn} = 0.46). These correspond to the 8th to 11th patterns within the red box of Fig. 6(a). The system's resolution exhibits a positive correlation with the illumination NA. The theoretical maximum resolution, derived from actual system parameters, is 567 nm, aligning with element 5 in group 9 (615 nm) of the USAF target, affirming the nominal value.

In Sec. III C, it was noted that dark-field sub-aperture positioning can be achieved with a reduced number of LEDs. Figure 6(e) illustrates the reconstruction results using 16, 8, and 4 LEDs. Cross-sectional profiling reveals that the three correction methods consistently resolve features down to element 5 in group 9 (615 nm),

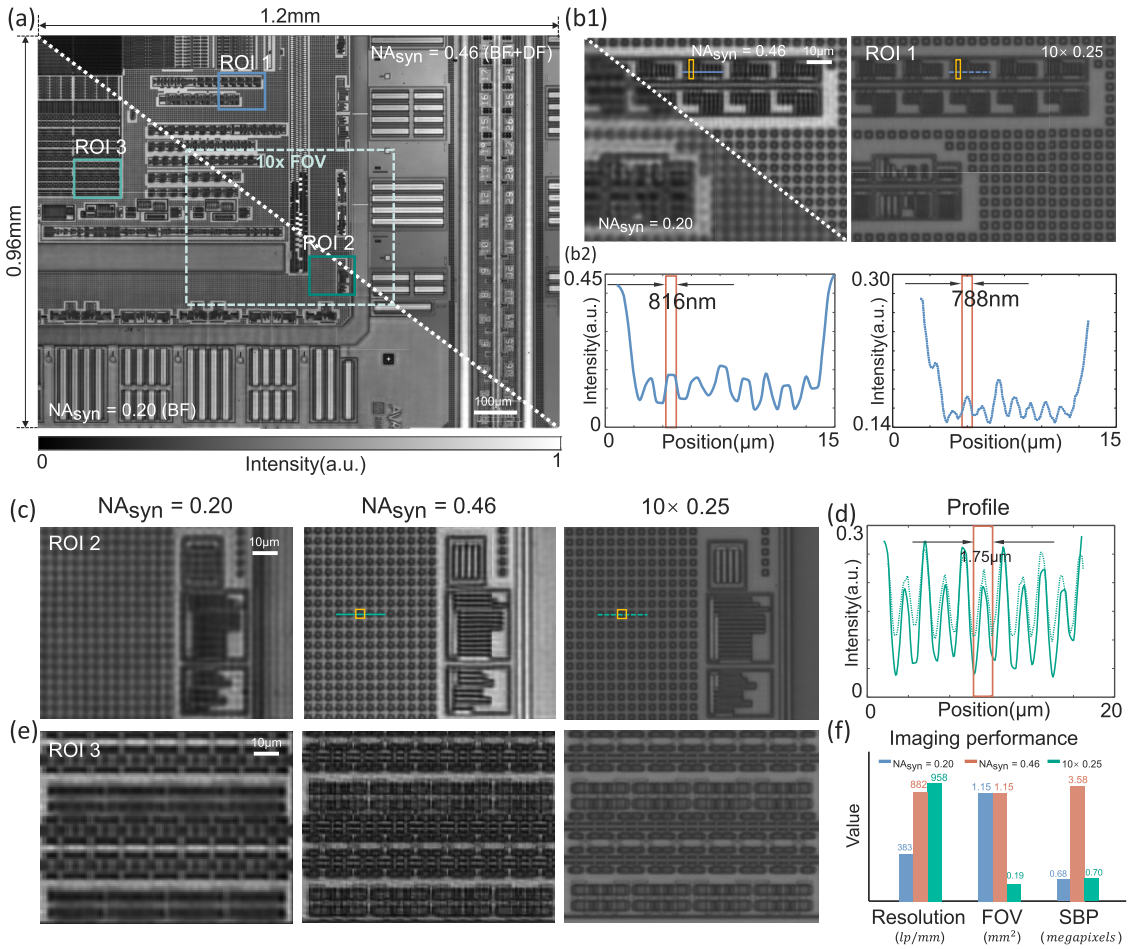

FIG. 7. Reconstruction results of the SMIC SM27 series chips' intensity images. (a) Full field reconstruction (1.2 × 0.96 mm^2), containing the comparison of the reconstructed intensity results between bright-field (NA_{syn} = 0.2) and the addition of dark-field (NA_{syn} = 0.46). (b) Magnified view of ROI1: intensity comparison (NA_{syn} = 0.2, NA_{syn} = 0.46, 10 × 0.25 NA) and section line comparison (NA_{syn} = 0.46 vs 10 × 0.25 NA). (c) and (e) Magnified views of ROI2 and ROI3: intensity comparison (NA_{syn} = 0.2, NA_{syn} = 0.46, 10 × 0.25 NA). (d) Section line comparison (NA_{syn} = 0.46 vs 10 × 0.25 NA) from (c). (f) Imaging performance comparison.

reaching their theoretical resolution. These results demonstrate that for a USAF target, the simplified method's correction does not compromise the system's resolution limit. This outcome is linked to the high-frequency distribution characteristics of the object's spectrum. This finding indicates that in reflective FPM systems, the USAF target could be used first to correct LED positioning errors before imaging complex industrial samples.

B. Chip inspection

Modern chip processing and manufacturing epitomize the pinnacle of industrial technology. The production process encompasses a sequence of precise stages from pre-design, wafer preparation, photolithography, etching, metallization to packaging and testing. To guarantee chip performance and reliability, each manufacturing step necessitates stringent control over process accuracy and completion. This entails not only the utilization of manufacturing equipment with exceptionally high processing precision but also the incorporation of various advanced detection methods throughout the entire production line to achieve comprehensive process quality control. To validate the correction capability of dmc-rFPM in practical scenarios and the improvements in detection accuracy and efficiency enabled by precise FPM reconstruction, this study investigates SMIC's SM27 series chips using dark-field-incorporated FPM reconstruction. Through the dmc-rFPM correction of dark-field sub-apertures, we successfully achieved high-throughput microscopic imaging. Figure 7(a) presents the FOV for the 4× objective and the 10× objective. The FOV of the 4× objective is divided by a diagonal dotted line. The lower left portion shows the FPM-reconstructed intensity with only bright-field data, while the upper right portion presents reconstruction incorporating dark-field information. Figures 7(b1), 7(c), and 7(e) provide magnified views of ROI1, ROI2, and ROI3, respectively, from Fig. 7(a), which enable a direct comparison of resolution improvements achieved by incorporating dark-field imaging.

Figure 7(b1) displays the structures of the polysilicon gate and metal interconnects. The primary role of the polysilicon gate is to establish a channel through electric field manipulation to regulate the opening and closing of the MOSFET, thereby controlling the current flow. The metal interconnect line serves to facilitate electrical connections among various components for signal transmission. These structures are crucial in influencing the performance and integration of the chip.[36–38] Conventional manufacturing processes impose stringent criteria regarding the dimensions (width and length) and uniformity of both components. Adherence to these specifications is imperative to ensure the electrical integrity of the final product. Figure 7(b1) depicts the direct imaging of the partial FOV shown in ROI1 using a 10× 0.25 NA microscope objective. The width of the detected structure, as observed from the intensity section line result in Fig. 7(b2), measures ~816 nm, aligning closely with the nominal value of 800 nm. The results obtained from FPM reconstruction were in agreement with those from direct imaging using a 10×0.25 NA objective. In addition, Fig. 7(c) illustrates the array arrangement structure, typically comprising memory cells, logic gates, or dummies for structural testing. Such components require highly regular array configurations, which directly impact the chip's stability, operational performance, and power consumption.[39–41] In addition, morphological defects in these structures can lead to functional failures, such as localized hot spots or excessive resistance.[42,43] Conventional inspection methods struggle to simultaneously observe large quantities of microstructures, whereas FPM's intrinsic properties are uniquely suited for high-resolution imaging of fine structures across large FOVs. The section lines in Fig. 7(d) indicate that by incorporating dark-field information, FPM can resolve fine structural details and achieve resolution comparable to that of high-magnification objectives. Figure 7(f) shows the comparison of the imaging capabilities of three different modes. The results indicate that the proposed system achieves an SBP of up to 3.58 megapixels, representing a fivefold improvement over traditional imaging modes. After system parameter calibration, FPM enables simultaneous observation of tens of thousands of regularly arranged microstructures within the field of view of a 4×0.1 NA objective, demonstrating a sixfold improvement in imaging throughput compared to conventional imaging using a 10× 0.25 NA objective. For components needing synchronous detection of appearance and positional arrangement, FPM's high-throughput capability significantly enhances detection efficiency.

V. SUMMARY AND DISCUSSION

This work proposes dmc-rFPM, a dark-field sub-aperture correction method based on reflective FPM, which uses SSIM as the evaluation metric. This method resolves the critical limitation of conventional transmissive FPM correction methods, which fail to adapt to reflective FPM. The cost function, based on SSIM, exhibits a residual distribution characteristic that ensures a globally unique solution. Unlike conventional correction methods, the proposed method eliminates the need for iterative reconstruction of dark-field information during the correction process, resulting in significantly reduced time consumption. Moreover, it reduces the required number of sub-apertures and leverages parallel processing with GPU acceleration to further enhance correction speed. Simulations are also employed to evaluate the correction capability of dmc-rFPM under varying error magnitudes. The results demonstrate that the deviation between the dmc-rFPM-corrected output and the ground truth is negatively proportional to the number of LEDs used and positively proportional to the rotation angle. Furthermore, the effectiveness of dmc-rFPM is confirmed through FPM reconstruction experiments conducted on the standard USAF target and SMIC chip.

The high imaging throughput of FPM systems holds significant potential for enhancing industrial detection efficiency. Moreover, their simple structure can streamline production lines and reduce manufacturing costs, making them highly promising for industrial applications. The proposed method in this work decouples correction from reconstruction and establishes a stable sub-aperture error cost function, thus enabling robust and rapid correction along with high-throughput imaging during practical detection. This approach effectively improves online detection efficiency. Particularly suited for batch industrial detection, the method ensures imaging quality while reducing computational overhead, thereby meeting the stringent real-time and stability requirements of production lines.

SUPPLEMENTARY MATERIAL

More details on visualizations are provided in the supplementary materials.

ACKNOWLEDGMENTS

This work was supported by the National Natural Science Foundation of China (Grant Nos. 62227818, 62361136588, 62305162, and U21B2033), National Key Research and Development Program of China (Grant Nos. 2022YFA1205002, 2024YFE0101300, 2024YFF0505603, and 2024YFF0505600), Biomedical Competition Foundation of Jiangsu Province (Grant No. BE2022847), Key National Industrial Technology Cooperation Foundation of Jiangsu Province (Grant No. BZ2022039), Fundamental Research Funds for the Central Universities (Grant No. 30923010206), Fundamental Research Funds for the Central Universities (Grant Nos. 2023102001 and 2024202002), National Key Laboratory of Plasma Physics (Grant No. JCKYS2024212804), and Open Research Fund of Jiangsu Key Laboratory of Spectral Imaging and Intelligent Sense (Grant Nos. JSGP202105, JSGP202201, and JSGPCXZNGZ202401), China Postdoctoral Science Foundation (Grant Nos. 2023TQ0160 and 2023M731683), Fundamental Research Funds for the Central Universities (Grant No. 30923010305), and Project No. WPC3/2022/47/INTENCITY/2024 funded by the National Centre for Research and Development (NCBR) under the third Polish-Chinese/Chinese-Polish Joint Research Call (2022).

AUTHOR DECLARATIONS

Conflict of Interest

The authors have no conflicts to disclose.

Author Contributions

Rui Gao: Conceptualization (equal); Data curation (lead); Formal analysis (lead); Investigation (lead); Methodology (equal); Software (lead); Validation (lead); Visualization (lead); Writing – original draft (lead); Writing – review & editing (equal). **Jiasong Sun**: Conceptualization (equal); Funding acquisition (equal); Investigation (equal); Methodology (equal); Project administration (equal); Resources (equal); Supervision (equal); Writing – review & editing (equal). **Yao Fan**: Visualization (equal); Writing – review & editing (equal). **Yefeng Shu**: Visualization (equal); Writing – review & editing (equal). **Maciej Trusiak**: Writing – review & editing (equal). **Qian Chen**: Funding acquisition (lead); Resources (lead). **Chao Zuo**: Funding acquisition (lead); Project administration (lead); Resources (lead).

DATA AVAILABILITY

The data that support the findings of this study are available from the corresponding author upon reasonable request.

REFERENCES

[1] B. Ma, T. Zimmermann, M. Rohde, S. Winkelbach, F. He, W. Lindenmaier, and K. E. J. Dittmar, "Use of autostitch for automatic stitching of microscope images," Micron **38**, 492–499 (2007).

[2] J. Chalfoun, M. Majurski, T. Blattner, K. Bhadriraju, W. Keyrouz, P. Bajcsy, and M. Brady, "Mist: Accurate and scalable microscopy image stitching tool with stage modeling and error minimization," Sci. Rep. **7**, 4988 (2017).

[3] J. Li, L. Ma, Y. Fan, N. Wang, K. Duan, Q. Han, X. Zhang, G. Su, C. Li, and L. Tang, "An image stitching method for airborne wide-swath hyperspectral imaging system equipped with multiple imagers," Remote Sens. **13**, 1001 (2021).

[4] T. M. Turpin, L. H. Gesell, J. Lapides, and C. H. Price, "Theory of the synthetic aperture microscope," Proc. SPIE **2566**, 230–240 (1995).

[5] T. S. Ralston, D. L. Marks, P. Scott Carney, and S. A. Boppart, "Interferometric synthetic aperture microscopy," Nat. Phys. **3**, 129–134 (2007).

[6] P. Gao and C. Yuan, "Resolution enhancement of digital holographic microscopy via synthetic aperture: A review," Light: Adv. Manuf. **3**, 105–120 (2022).

[7] G. Zheng, R. Horstmeyer, and C. Yang, "Wide-field, high-resolution Fourier ptychographic microscopy," Nat. Photonics **7**, 739–745 (2013).

[8] X. Ou, G. Zheng, and C. Yang, "Embedded pupil function recovery for Fourier ptychographic microscopy," Opt. Express **22**, 4960–4972 (2014).

[9] P. Song, S. Jiang, H. Zhang, X. Huang, Y. Zhang, and G. Zheng, "Full-field Fourier ptychography (FFP): Spatially varying pupil modeling and its application for rapid field-dependent aberration metrology," APL Photonics **4**, 050802 (2019).

[10] H. Lee, B. H. Chon, and H. K. Ahn, "Rapid misalignment correction method in reflective Fourier ptychographic microscopy for full field of view reconstruction," Opt. Lasers Eng. **138**, 106418 (2021).

[11] V. H. Pham, B. H. Chon, and H. K. Ahn, "Whale optimization algorithm-based parallel computing for accelerating misalignment estimation of reflective Fourier ptychography microscopy," IEEE Photonics J. **15**, 7800109 (2023).

[12] X. Ou, R. Horstmeyer, G. Zheng, and C. Yang, "High numerical aperture Fourier ptychography: Principle, implementation and characterization," Opt. Express **23**, 3472–3491 (2015).

[13] K. S. Park, Y. S. Bae, S.-S. Choi, and M. Y. Sohn, "High numerical aperture reflective deep ultraviolet Fourier ptychographic microscopy for nanofeature imaging," APL Photonics **7**, 096105 (2022).

[14] L. Tian, X. Li, K. Ramchandran, and L. Waller, "Multiplexed coded illumination for Fourier ptychography with an LED array microscope," Biomed. Opt. Express **5**, 2376–2389 (2014).

[15] Y. Fan, J. Sun, Y. Shu, Z. Zhang, G. Zheng, W. Chen, J. Zhang, K. Gui, K. Wang, Q. Chen *et al.*, "Efficient synthetic aperture for phaseless Fourier ptychographic microscopy with hybrid coherent and incoherent illumination," Laser Photonics Rev. **17**, 2200201 (2023).

[16] L.-H. Yeh, J. Dong, J. Zhong, L. Tian, M. Chen, G. Tang, M. Soltanolkotabi, and L. Waller, "Experimental robustness of Fourier ptychography phase retrieval algorithms," Opt. Express **23**, 33214–33240 (2015).

[17] S. Zhang, A. Wang, J. Xu, T. Feng, J. Zhou, and A. Pan, "FPM-WSI: Fourier ptychographic whole slide imaging via feature-domain backdiffraction," Optica **11**, 634–646 (2024).

[18] A. Williams, J. Chung, X. Ou, G. Zheng, S. Rawal, Z. Ao, R. Datar, C. Yang, and R. Cote, "Fourier ptychographic microscopy for filtration-based circulating tumor cell enumeration and analysis," J. Biomed. Opt. **19**, 066007 (2014).

[19] Z. Li, Y. Shu, L. Lu, J. Sun, Q. Shen, P. Gao, P. Zdańkowski, M. Trusiak, M. Kujawinska, Q. Chen *et al.*, "Fourier holo-ptychographic microscopy: A hybrid digital holography-Fourier ptychography approach to synthetic-aperture quantitative phase microscopy," ACS Photonics **12**, 2965 (2025).

[20] M. Liang, C. Bernadt, S. B. J. Wong, C. Choi, R. Cote, and C. Yang, "All-in-focus fine needle aspiration biopsy imaging based on Fourier ptychographic microscopy," J. Pathol. Inf. **13**, 100119 (2022).

[21] H. Lee, B. H. Chon, and H. K. Ahn, "Reflective Fourier ptychographic microscopy using a parabolic mirror," Opt. Express **27**, 34382–34391 (2019).

[22] G. Zheng, C. Shen, S. Jiang, P. Song, and C. Yang, "Concept, implementations and applications of Fourier ptychography," Nat. Rev. Phys. **3**, 207–223 (2021).

[23] H. Wang, J. Zhu, J. Sung, G. Hu, J. Greene, Y. Li, S. Park, W. Kim, M. Lee, Y. Yang *et al.*, "Fourier ptychographic topography," Opt. Express **31**, 11007–11018 (2023).

[24] K. Guo, S. Dong, and G. Zheng, "Fourier ptychography for brightfield, phase, darkfield, reflective, multi-slice, and fluorescence imaging," IEEE J. Sel. Top. Quantum Electron. **22**, 77–88 (2015).

[25] S. Pacheco, G. Zheng, and R. Liang, "Reflective Fourier ptychography," J. Biomed. Opt. **21**, 026010 (2016).

[26] J. Sun, Q. Chen, Y. Zhang, and C. Zuo, "Efficient positional misalignment correction method for Fourier ptychographic microscopy," Biomed. Opt. Express **7**, 1336–1350 (2016).

[27]R. Eckert, Z. F. Phillips, and L. Waller, "Efficient illumination angle self-calibration in Fourier ptychography," Appl. Opt. **57**, 5434–5442 (2018).
[28]Z. Wang, A. C. Bovik, H. R. Sheikh, and E. P. Simoncelli, "Image quality assessment: From error visibility to structural similarity," IEEE Trans. Image Process. **13**, 600–612 (2004).
[29]M. A. Fischler and R. C. Bolles, "Random sample consensus: A paradigm for model fitting with applications to image analysis and automated cartography," Commun. ACM **24**, 381–395 (1981).
[30]J. Sun, C. Zuo, J. Zhang, Y. Fan, and Q. Chen, "High-speed Fourier ptychographic microscopy based on programmable annular illuminations," Sci. Rep. **8**, 7669 (2018).
[31]Y. Shu, J. Sun, J. Lyu, Y. Fan, N. Zhou, R. Ye, G. Zheng, Q. Chen, and C. Zuo, "Adaptive optical quantitative phase imaging based on annular illumination Fourier ptychographic microscopy," PhotoniX **3**, 24 (2022).
[32]N. Hussain, M. Hasanzade, D. W. Breiby, and M. N. Akram, "Performance comparison of wavelet families for noise reduction and intensity thresholding in Fourier ptychographic microscopy," Opt. Commun. **519**, 128400 (2022).
[33]D. R. I. M. Setiadi, "PSNR vs SSIM: Imperceptibility quality assessment for image steganography," Multimedia Tools Appl. **80**, 8423–8444 (2021).
[34]S. Tang, F. He, X. Huang, and J. Yang, "Online PCB defect detector on a new PCB defect dataset," arXiv:1902.06197 (2019).
[35]B. Rühle, J. F. Krumrey, and V.-D. Hodoroaba, "Workflow towards automated segmentation of agglomerated, non-spherical particles from electron microscopy images using artificial neural networks," Sci. Rep. **11**, 4942 (2021).
[36]M.-J. Tsai, K.-H. Peng, C.-J. Sun, S.-C. Yan, C.-C. Hsu, Y.-R. Lin, Y.-H. Lin, and Y.-C. Wu, "Fabrication and characterization of stacked poly-si nanosheet with gate-all-around and multi-gate junctionless field effect transistors," IEEE J. Electron Devices Soc. **7**, 1133–1139 (2019).
[37]W. C.-Y. Ma and Y.-H. Chen, "Performance improvement of poly-Si tunnel FETs by trap density reduction," IEEE Trans. Electron Devices **63**, 864–868 (2015).
[38]G. Jerke and J. Lienig, "Hierarchical current density verification for electromigration analysis in arbitrarily shaped metallization patterns of analog circuits," in *Proceedings 2002 Design, Automation and Test in Europe Conference and Exhibition* (IEEE, 2002), pp. 464–469.
[39]J. P. Rojas, G. A. Torres Sevilla, M. T. Ghoneim, S. B. Inayat, S. M. Ahmed, A. M. Hussain, and M. M. Hussain, "Transformational silicon electronics," ACS Nano **8**, 1468–1474 (2014).
[40]Y. Y. Chen, R. Degraeve, S. Clima, B. Govoreanu, L. Goux, A. Fantini, G. S. Kar, G. Pourtois, G. Groeseneken, D. J. Wouters *et al.*, "Understanding of the endurance failure in scaled HfO_2-based 1T1R RRAM through vacancy mobility degradation," in *2012 International Electron Devices Meeting* (IEEE, 2012), pp. 20–23.
[41]B. Govoreanu, A. Redolfi, L. Zhang, C. Adelmann, M. Popovici, S. Clima, H. Hody, V. Paraschiv, I. Radu, A. Franquet *et al.*, "Vacancy-modulated conductive oxide resistive RAM (VMCO-RRAM): An area-scalable switching current, self-compliant, highly nonlinear and wide on/off-window resistive switching cell," in *2013 IEEE International Electron Devices Meeting* (IEEE, 2013), pp. 10–12.
[42]C. Mack, *Fundamental Principles of Optical Lithography: The Science of Microfabrication* (John Wiley & Sons, 2008).
[43]Y. Liu, C. Zeng, J. Yu, J. Zhong, B. Li, Z. Zhang, Z. Liu, Z. M. Wang, A. Pan, and X. Duan, "Moiré superlattices and related moiré excitons in twisted van der Waals heterostructures," Chem. Soc. Rev. **50**, 6401–6422 (2021).